PNAS RESEARCH ARTICLE | CHEMISTRY

Facilely tuning the intrinsic catalytic sites of the spinel oxide for peroxymonosulfate activation: From fundamental investigation to pilot-scale demonstration

Mingjie Huang[a], Yu-Sheng Li[a], Chuan-Qi Zhang[b], Chao Cui[a], Qing-Qing Huang[c], Mengkai Li[d], Zhimin Qiang[d], Tao Zhou[e], Xiaohui Wu[e], and Han-Qing Yu[a,1]

Edited by Alexis Bell, University of California, Berkeley, Berkeley, CA; received February 14, 2022; accepted April 30, 2022

Heterogeneous peroxymonosulfate (PMS)–based advanced oxidation processes (AOPs) have shown a great potential for pollutant degradation, but their feasibility for large-scale water treatment application has not been demonstrated. Herein, we develop a facile coprecipitation method for the scalable production (~10 kg) of the Cu-Fe-Mn spinel oxide (CuFeMnO). Such a catalyst has rich oxygen vacancies and symmetry-breaking sites, which endorse it with a superior PMS-catalytic capacity. We find that the working reactive species and their contributions are highly dependent on the properties of target organic pollutants. For the organics with electron-donating group (e.g., -OH), high-valent metal species are mainly responsible for the pollutant degradation, whereas for the organics with electron-withdrawing group (e.g., -COOH and -NO_2), hydroxyl radical (•OH) as the secondary oxidant also plays an important role. We demonstrate that the CuFeMnO–PMS system is able to achieve efficient and stable removal of the pollutants in the secondary effluent from a municipal wastewater plant at both bench and pilot scales. Moreover, we explore the application prospect of this PMS-based AOP process for large-scale wastewater treatment. This work describes an opportunity to scalably prepare robust spinel oxide catalysts for water purification and is beneficial to the practical applications of the heterogeneous PMS-AOPs.

advanced oxidation process | peroxymonosulfate | catalysis | water treatment | large-scale

Advanced oxidation process (AOP) based on peroxymonosulfate (PMS) is a promising technology for water pollution control. Such an attractive technology has seen a rapid development due to its several compelling advantages over the conventional Fenton system, such as the fast heterogeneous reaction rate and the outstanding performance in a wider pH range (2 to 10 vs. 2 to 5 for Fenton reaction) (1–3). Among the various PMS activation methods, transition metal oxide (M_xO_y) has become the best option owing to its low energy requirement, operational convenience, and easy postreaction recovery (4). These remarkable merits endow the M_xO_y catalysts with a great potential for practical application. To date, great efforts have been engaged to elucidate the reaction characteristics (i.e., kinetics and mechanisms) of the M_xO_y/PMS systems in the laboratory (5). However, the attempts to put such a highly efficient heterogeneous AOP to practical application (even at pilot scale) is scarcely.

One obstacle for the large-scale application of the PMS-AOP is the difficulty in balancing the catalytic capacity and production quantity of the M_xO_y catalysts. Recently, research interests have been focused on the designation of various catalysts for PMS activation, such as the defect-engineered Co_3O_4 with porous multishelled hollow architecture (MS-VO-Co_3O_4) (6), ultrathin Fe_3O_4 nanosheets (2D Fe_3O_4) (7), $Co(OH)_2$ hollow microsphere supported titanate nanotubes (CoM/TNTs) (8), etc. However, these fancy nano-sized materials could not fulfill the goals in a commercially viable way due to their low yield, usually in milligram scale, although they show impressive catalytic performance for PMS activation. In contrast, the coprecipitation method has the advantages of easy operation and feasibility of large-scale manufacturing (i.e., kilogram scale). However, the coprecipitation products often possess a broad size distribution, and also lack well-designed microstructure or reactive sites, leading to the inferior catalytic capacity compared to the nano-sized catalysts obtained in other protocols with controllable crystallization (9–12). Thus, from a practical viewpoint, it is of great practical importance to fabricate the highly efficient M_xO_y catalysts using the simple coprecipitation method.

Such an objective can be attained by changing the intrinsic composition of M_xO_y catalysts (i.e., the number of metal species and stoichiometric ratio of the metal ions) in the coprecipitation process. Generally, bimetallic or trimetallic M_xO_y catalysts show

Significance

Heterogeneous peroxymonosulfate (PMS)–based advanced oxidation process (AOP) has been extensively tested for water purification, but its application feasibility at large scale has not been validated. Here, we develop a facile coprecipitation method for the scalable production (~10 kg) of the nonstoichiometric Cu-Fe-Mn spinel oxide (CuFeMnO) catalyst with a great PMS-activation capacity. The mechanisms for the robust PMS-catalytic ability of this catalyst are elucidated with a suite of experiments and theoretical calculations. Furthermore, the application feasibility of applying the CuFeMnO-PMS AOP for water treatment at both bench and pilot scales is demonstrated. This work validates the great potential of scalable preparation for the nonstoichiometric CuFeMnO catalyst and provides a conceptual advance to design robust and practical PMS-based catalytic systems for water purification.

Author contributions: H.-Q.Y. designed research; M.H., Y.-S.L., C.-Q.Z., C.C., and Q.-Q.H. performed research; M.H., Y.-S.L., Q.-Q.H., M.L., Z.Q., T.Z., and H.-Q.Y. contributed new reagents/analytic tools; M.H., Y.-S.L., C.-Q.Z., C.C., M.L., Z.Q., T.Z., X.W., and H.-Q.Y. analyzed data; and M.H. and H.-Q.Y. wrote the paper.

The authors declare no competing interest.

This article is a PNAS Direct Submission.

[1]To whom correspondence may be addressed. Email: hqyu@ustc.edu.cn.

This article contains supporting information online at http://www.pnas.org/lookup/suppl/doi:10.1073/pnas.2202682119/-/DCSupplemental.

Published July 18, 2022.

a higher activity for PMS activation than monometallic ones. Such an activity enhancement is attributed to several factors, such as the increased surface hydroxyl group (13), synergetic electron-transfer between different metals (14), and the enhanced metal-oxygen covalency in octahedral configuration of spinel or perovskite oxides (15, 16). In addition to the above-described multimetallic protocol, another effective strategy is to fabricate oxygen vacancies (OVs) -rich catalysts through the coprecipitation of the nonstoichiometric mixed metal precursors (17). The redox-active OVs with electron-rich character could enhance the adsorption and activation of PMS, and thereby improve the degradation performance of organic pollutants (18). Thus, the rational integration of these two strategies paves the way for the scale production of highly efficient PMS-activation catalysts via the facile coprecipitation method. However, the catalytic mechanism of the nonstoichiometric multimetallic catalysts for PMS activation remains unrevealed, and its scale-up treatment performance for practical application needs to be further investigated.

In this work, a facile eco-friendly coprecipitation method was adopted to fabricate the nonstoichiometric ternary $CuFeMnO_4$ spinel oxide (CuFeMnO) for water decontamination via PMS activation. First, the composition, microstructure, and morphological features of the synthesized CuFeMnO catalyst were examined. Then, the catalytic activity of CuFeMnO was evaluated and the underlying mechanism for its PMS-catalytic capacity was elucidated. Subsequently, the reactive species and their specific contributions to organic degradation were identified. Finally, the application feasibility of the CuFeMnO/PMS system for real water treatment was demonstrated at pilot scale.

1. Results and Discussion

1.1 Physicochemical Properties of the CuFeMnO Catalyst. The crystalline structure of the gram-scale CuFeMnO catalyst was identified by X-ray diffraction (XRD) analysis (Fig. 1*A*). Most of the diffraction peaks were identical to those of $CuFeMnO_4$ spinel oxide (Joint Committee Powder Diffraction Standards No. 20-0358), with neglectable CuO impurity observed. The N_2 adsorption–desorption isotherm with a hysteresis loop corresponded to the typical IV-type characteristic (Fig. 1*B*), indicating the mesoporous structure of the CuFeMnO catalyst (19). The Brunauer-Emmett-Teller (BET) surface area and average pore size were measured to be 146.3 m^2/g and 2.3 nm, respectively. In addition, the scanning electron microscopy (SEM) image clearly shows the aggregation of the individual CuMnFeO nanosphere (Fig. 1*C*), which possessed an average size of ~40 nm as depicted in the transmission electron microscopy (TEM) image (Fig. 1*D*). The high-resolution TEM (HR-TEM) pattern in Fig. 1*E* indicates the single-crystalline structure of the CuFeMnO with the lattice fingers of 0.245 and 0.294 nm, which were correlated with the $d_{(222)}$ and $d_{(220)}$ spacing of the $CuMnFeO_4$ spinel oxide, respectively. As displayed in the TEM-EDS element mapping images (Fig. 1*F*), the Cu, Fe, and Mn elements were homogeneously distributed over the nanospheres. Furthermore, the inductively coupled plasma-atomic emission spectrometry (ICP-AES) result shows that the atomic ratio of Cu, Fe, and Mn in the product was ~2.0:2.4:1. Thus, the chemical formula of the catalyst can be denoted as $Cu_{1.1}Fe_{1.34}Mn_{0.56}O_4$, indicating a nonstoichiometric character of the synthesized ternary CuFeMnO catalyst.

1.2 Evaluation of Catalytic Activity. The superior PMS-catalytic capacity of the CuFeMnO catalyst was demonstrated for the rapid phenol degradation and total organic carbon (TOC) removal. As shown in Fig. 2, phenol removal of approximately 81.0% was achieved within 30 min with the CuFeMnO as the catalyst, while it was 76.4% for the ternary CoFeMnO spinel oxide and less than 58.0% for the binary (i.e., $CoFe_2O_4$, $CuFe_2O_4$, $MnFe_2O_4$, and $BiFeO_3$) or unary (i.e., Co_3O_4, Mn_3O_4, Mn_2O_3, MnO_2, Fe_2O_3, and CuO) metal oxides. In such a reaction process, negligible phenol was removed via the CuFeMnO adsorption or the direct PMS oxidation (*SI Appendix*, Fig. S1). Interestingly, the Cobased catalysts exhibited the best PMS-activation performance among the groups of homogeneous metal ions (20), binary or unary oxides (Fig. 2), but not in the ternary oxides group, suggesting the strong synergistic effect between Cu, Fe, and Mn ions in the CuFeMnO catalyst for PMS activation. Notably, the CuFeMnO/PMS achieved the highest removal efficiency of TOC (approximately 56.6%), whereas it was less than 40.0% for the other metal oxides studied (Fig. 2), and the catalytic capacity of the CuFeMnO catalyst could be further improved by optimizing its chemical composition (*SI Appendix*, Fig. S2). In addition, the

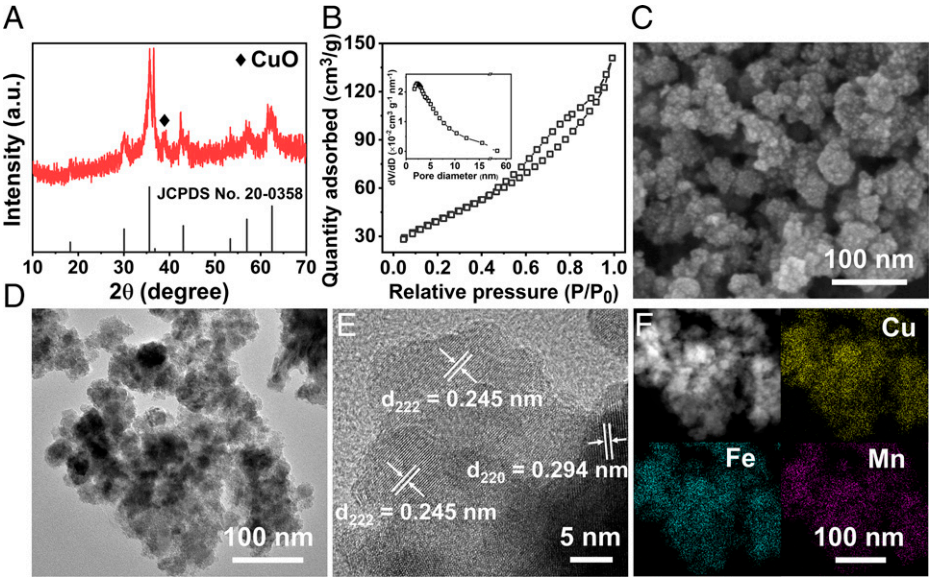

Fig. 1. Physicochemical properties of the CuFeMnO catalyst. (*A*) XRD pattern, (*B*) nitrogen adsorption-desorption isotherm, (*C*) SEM, (*D*) TEM, (*E*) HR-TEM, and (*F*) TEM-EDS mapping images of the CuFeMnO catalyst. The inset in (*B*) is the pore diameter distribution curve of the CuFeMnO.

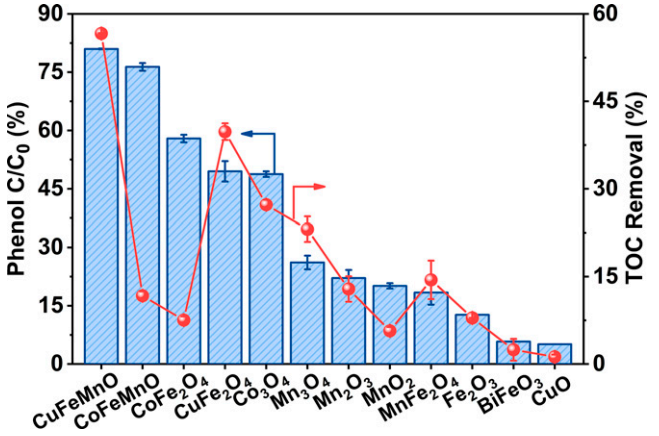

Fig. 2. The PMS-catalytic performance of the different M_xO_y catalysts for phenol degradation. Experimental conditions: [catalyst] = 0.2 g/L, [PMS] = 0.3 g/L, [phenol] = 0.3 mM, pH = 6.0, T = 25 ± 2 °C.

kilogram-scale CuFeMnO catalyst also exhibited a similar catalytic activity compared to the gram-scale CuFeMnO for phenol degradation and TOC removal (*SI Appendix*, Fig. S3). These results validate the superior catalytic ability of the nonstoichiometric multimetallic CuFeMnO catalyst synthesized via the facile coprecipitation method.

The stability and versatility of the CuFeMnO catalyst were then evaluated. The ICP-AES measurement shows that the leached Cu ion was 2.8 mg/L and no leached Fe or Mn ion was detected in the PMS-activation process. This result indicates the good stability of the CuFeMnO catalyst, which endowed the CuFeMnO catalyst with a high reusability over four consecutive cycles (*SI Appendix*, Fig. S4). As shown in *SI Appendix*, Fig. S5, phenol could be effectively degraded in a wide range of CuFeMnO dosage (0.05 to 0.4 g/L) and PMS concentration (0.1 to 0.5 g/L), also with high pH versatility (4.0 to 8.0). In addition, the PMS-activation performance of the ternary CuFeMnO catalyst was almost insusceptible to the wastewater matrix such as the common anions (e.g., Cl^-, NO_3^-, SO_4^{2-}, and HCO_3^-) and the natural organic matter (e.g., humic acid) (*SI Appendix*, Fig. S7). These results evidence that the highly efficient CuFeMnO catalyst had an application potential for real water decontamination.

1.3 Mechanism for the Superior PMS-Catalytic Capacity of CuFeMnO. A combination of characterizations and density functional theory (DFT) calculations was adopted to elucidate the mechanism for the superior PMS-catalytic capacity of the CuFeMnO. The X-ray photoelectron spectroscopy (XPS) analysis shows that the proportion of the low-valent metal species (e.g., Cu^I, Fe^{II}, and Mn^{II}/Mn^{III}) on the CuFeMnO surface were considerably higher than those of the $CuFe_2O_4$, CuO, α-Fe_2O_3, and Mn_2O_3 (Fig. 3*A* and *SI Appendix*, Fig. S8). These abundant surface electron-rich metal centers could be originated from the sufficient surface OVs, as verified by the electron paramagnetic resonance (EPR) studies. As shown in Fig. 3*B*, the distinctive response near g value of 2.030 was related to the typical signals of the unpaired electrons of the OVs (21). Also, the OV content of the CuFeMnO was much higher than that of the CuO, α-Fe_2O_3, and Mn_2O_3. These OVs or the unsaturated coordination metal sites could serve as efficient reaction sites for the adsorption and activation of PMS (18). The H_2-temperature programmed reduction (H_2-TPR) experiments were then conducted to validate the high reactivity of the OVs on the CuFeMnO catalyst by using H_2 as the probe molecule (Fig. 3*C*). Unary CuO showed almost a one-step

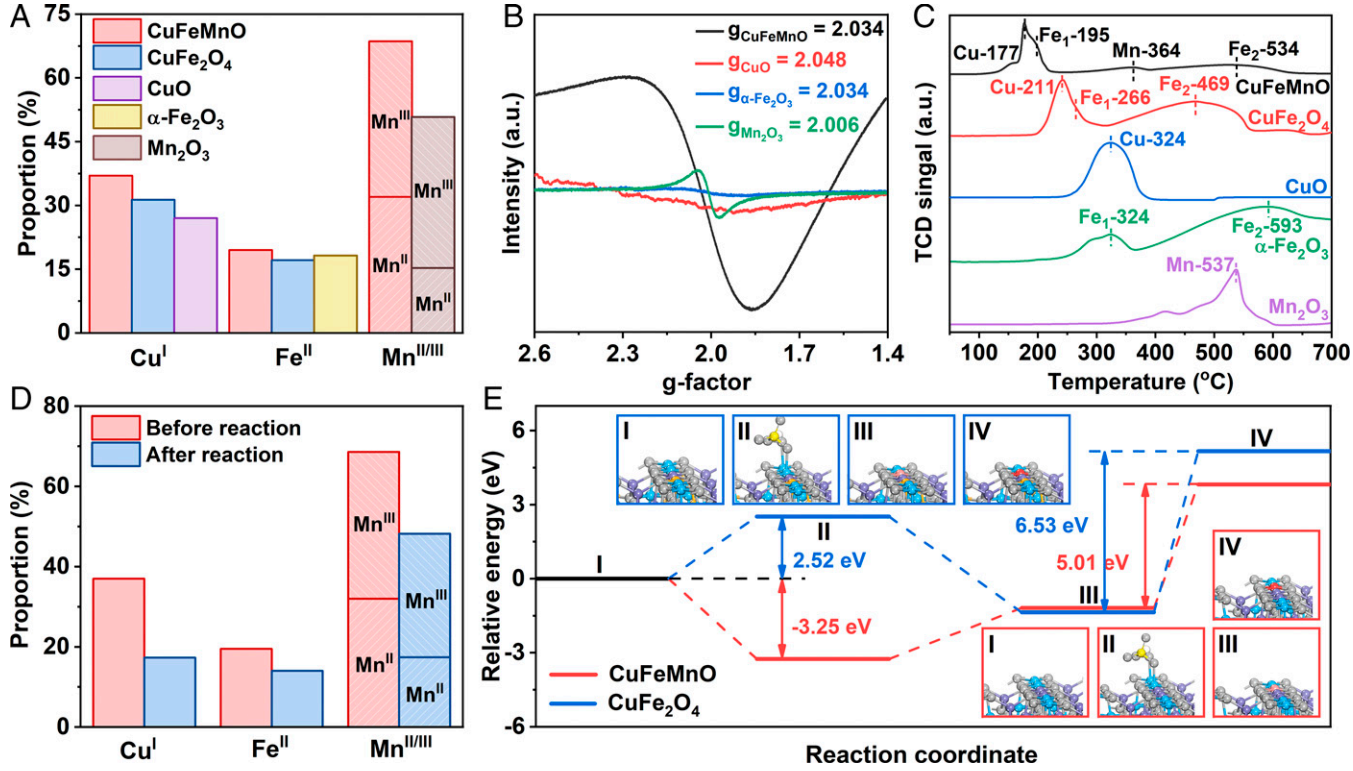

Fig. 3. Mechanism for the superior PMS-catalytic capacity of CuFeMnO. (*A*) The proportions of Cu^I, Fe^{II}, and Mn^{II}/Mn^{III} on the surface of the different metal oxides (e.g., CuFeMnO, $CuFe_2O_4$, CuO, α-Fe_2O_3, and Mn_3O_4) by XPS analysis. (*B*) The room-temperature EPR spectra of the different metal oxides. (*C*) H_2-TPR spectra of the different metal oxides. (*D*) The proportions of Cu^I, Fe^{II}, and Mn^{II}/Mn^{III} on the CuFeMnO surface before and after reaction. (*E*) The free energies for PMS activation by the CuFeMnO on the Cu sites (inset: corresponding intermediate structures).

reduction with the peak centers at 324 °C, which was ascribed to the reduction of Cu^{2+} to Cu^0 (22). Both α-Fe_2O_3 and Mn_2O_3 exhibited a clear two-step reduction process, which corresponded to the subsequent reduction from α-Fe_2O_3 to Fe_3O_4 and FeO and from Mn_2O_3 to Mn_3O_4 and MnO, respectively (23, 24). In comparison with these three unary metal oxides, the reduction peaks of Cu and Fe in the $CuFe_2O_4$ decreased drastically by 58 to 124 °C, and further decreased to lower temperatures on the CuFeMnO, indicating the high reactivity of the surface OVs on the CuFeMnO (25, 26). These results indicate that the nonstoichiometric feature endowed the ternary CuFeMnO catalyst with abundant surface OV sites, which boosted the adsorption and activation of PMS. Moreover, substantial decreases in the proportions of the surface Cu^I, Fe^{II}, and Mn^{II}/Mn^{III} on the CuFeMnO after the catalytic reactions were observed (Fig. 3*D* and *SI Appendix*, Fig. S9), suggesting the involvement of these metal species in affording electrons for the PMS activation.

DFT calculations were performed to further validate the synergistic effect among the three metal ions (i.e., Cu, Fe, and Mn) of the CuFeMnO in promoting PMS activation. Compared with the benchmark $CuFe_2O_4$ catalyst, the incorporation of Mn decreased the Mulliken charges of Cu and Fe by ~0.44e^- and 0.2e^-, respectively (*SI Appendix*, Fig. S10), suggesting the redistribution of the electrons on the ternary CuFeMnO catalyst. Such a prominent charge density gradient in a symmetry-breaking center was beneficial to PMS activation (27, 28), as confirmed by the DFT calculations. The heterogeneous metal oxide-based PMS activation process generally involved three steps: PMS adsorption on the metal site (II), and the subsequent reduction (III) and reoxidation (IV) of metal ion by PMS to generate reactive species (29, 30). As illustrated by the energy change plot for different steps (Fig. 3*E*), PMS was spontaneously adsorbed by the CuFeMnO with the adsorption energy of −3.25 eV on the Cu site, whereas this process was thermodynamically infeasible on the $CuFe_2O_4$. The incorporation of Mn can also substantially decrease the energy barrier for the reoxidation of Cu^I (from 6.53 to 5.01 eV) to their high-valent counterpart (i.e., Cu^{III}, discussed later). Meanwhile, in view of these three steps for PMS activation, the overall formation energy of Cu^{III} reduced from 5.16 to 3.82 eV after Mn was introduced. Similar result was also obtained when PMS was activated on the Fe site (*SI Appendix*, Fig. S11). A combination with the above characterization results suggests that the rich OVs and the symmetry-breaking sites on the nonstoichiometric ternary CuFeMnO spinel oxide were mainly responsible for its superior PMS-catalytic ability.

1.4 Reactive Species in the CuFeMnO/PMS System. EPR experiments were subsequently conducted to identify the reactive species in the CuFeMnO/PMS system. A typical seven-line EPR signal of 5,5-dimethyl-1-pyrrolidone-*N*-oxyl (DMPOX) was dominant in the coexistence of CuFeMnO and PMS, whereas negligible EPR signal was observed in the control experiments when CuFeMnO, PMS, or DMPO alone was presented (Fig. 4*A*). As reported, the formation of DMPOX could be resulted from the oxidation of DMPO by high-valent metals, immense amount of •OH suddenly generated, or $^1O_2$ (31–34). Therefore, comparative experiments were conducted to identify the reactive species responsible for the DMPOX generation, which also contributed mainly to the phenol degradation because of the significantly depressed signal intensity of DMPOX when phenol was introduced (Fig. 4*A*).

The radical quenching experiments show that different concentrations (approximately 0 to 500 mM) of ethanol (EA) and *tert*-butyl alcohol (TBA) had negligible effects on phenol degradation (*SI Appendix*, Fig. S12*A* and *B*), suggesting that both •OH and $SO_4^{\bullet-}$ were not generated in the CuFeMnO/PMS system. This was also confirmed by the EPR analysis, in which no substantial decrease in the signal intensity of DMPOX was observed when either EA or TBA was presented (Fig. 4*A*). In addition, the self-decomposition of PMS led to the generation of $^1O_2$ (35), which shows typical triplet EPR peaks with the intensity ratio of 1:1:1 (Fig. 4*B*). The peak intensity of $^1O_2$ considerably increased after the activation reaction of PMS by the CuFeMnO, whereas it remained unchanged when phenol was added (Fig. 4*B*), suggesting the minor contribution of $^1O_2$ to the phenol oxidation. These results show that the high-valent

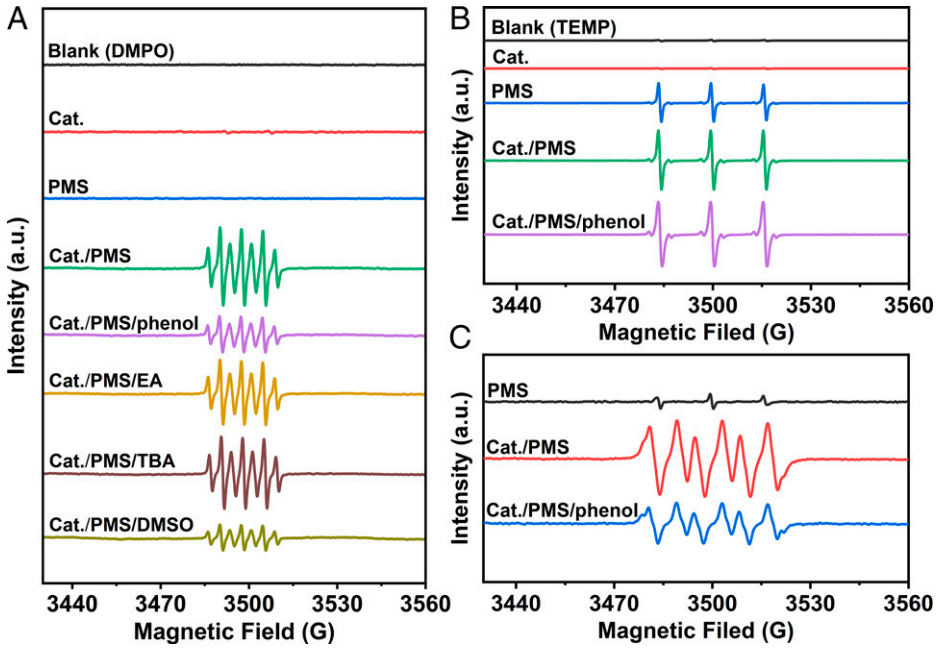

Fig. 4. Identification of the reactive species in the CuFeMnO/PMS system. EPR spectra of the different reaction systems with (*A*) DMPO in water, (*B*) TEMP in water, and (*C*) DMPO in methanol as the spin-trapping agents. Experimental conditions: [CuFeMnO] = 0.2 g/L, [PMS] = 0.3 g/L, [PH] = 0.3 mM, [DMPO] = [TEMP] = 50 mM, [EA] = [TBA] = [DMSO] = 0.5 M, pH = 6.0, T = 25 ± 2 °C.

metals (i.e., Cu^{III}, Fe^{IV}, or Mn^{V}) were responsible for the phenol degradation and DMPOX generation in the CuFeMnO/PMS system. To verify this conclusion, dimethyl sulfoxide (DMSO) was used as the effective scavenger for the high-valent metals (i.e., Cu^{III}, Fe^{IV}, or Mn^{V}) (36–38). *SI Appendix*, Fig. S12*C* shows that DMSO at a low concentration (approximately 10 mM) completely inhibited the phenol degradation. It should be noted that DMSO can directly react with PMS ($k_{PMS,\ DMSO} = 18 \pm 0.7\ M^{-1}\ s^{-1}$) (39), but the catalytic activation of PMS by the CuFeMnO in the presence of DMSO was still observed, because the decomposition rate of PMS in the mixed CuFeMnO/DMSO system was largely higher than that in DMSO alone (*SI Appendix*, Fig. S12*D*). Thus, the DMSO quenching experiment validates the critical role of the high-valent metals in the phenol degradation in the CuFeMnO/PMS system. This was also verified by the substantial decrease in the EPR peak intensity of DMPOX when DMSO was introduced (Fig. 4*A*). Moreover, the potential role of $O_2^{\bullet-}$ in the phenol degradation was also noticed, as the peak intensity of $O_2^{\bullet-}$ (the sextet EPR peak) was suppressed with the addition of phenol (Fig. 4*C*). Then, the contribution of $O_2^{\bullet-}$ to the phenol degradation was quantified using the *p*-nitro-blue tetrazolium chloride (NBT) method. As shown in *SI Appendix*, Fig. S13, the absorbance of NBT at 259 nm drastically increased within the initial 10 min. The calculated maximum $O_2^{\bullet-}$ concentration was ~26.5 μM at 0.2 g/L of CuFeMnO (*SI Appendix*, Fig. S14), which was equivalent to 10.9% of the degraded phenol under the same reaction conditions, indicating the minor role of $O_2^{\bullet-}$ in the phenol degradation. These results clearly demonstrate that the high-valent metals (i.e., Cu^{III}, Fe^{IV}, or Mn^{V}) were the dominant reactive species responsible for the phenol degradation in the CuFeMnO/PMS system.

1.5 Contribution of Different High-Valent Metals to Pollutant Degradation. Although the high-valent metals species (i.e., Cu^{III}, Fe^{IV}, or Mn^{V}) were found to be responsible for the phenol degradation in the CuFeMnO/PMS system, their individual contributions to pollutant degradation were unclear yet. Herein, methyl phenyl sulfoxide (PMSO) was used as a chemical probe to distinguish between Fe^{IV}/Mn^{V} and Cu^{III} species due to their marked difference in product formation. Fe^{IV}/Mn^{V} can oxidize PMSO to methyl phenyl sulfone ($PMSO_2$) through the oxygen transfer pathway (37, 40), while such a product is not formed through Cu^{III} oxidation, as Cu^{III} fails to form the stable metal-oxo species (41). As shown in *SI Appendix*, Figs. S15–S17, the CuFeMnO dosage, PMS concentration, and initial pH had notable effects on the PMSO oxidation and $PMSO_2$ formation. In such a reaction system, PMSO could be degraded through three pathways: the oxidative degradation by PMS and Fe^{IV}/Mn^{V} to generate $PMSO_2$, and by Cu^{III} to generate biphenyl compounds or hydroxylated products (42). We considered the rapid consumption of PMS in the CuFeMnO/PMS/PMSO system (*SI Appendix*, Fig. S12D), and the experimental data at 2 min were adopted to calculate the contributions of the above three pathways to the PMSO oxidation. Fig. 5*A* shows that, when the CuFeMnO dosage was increased from 0.1 to 0.4 g/L, the contributions of the high-valent metals substantially increased. However, interestingly, the proportion of Cu^{III} oxidation (excluding the role of PMS oxidation) changed slightly in a narrow range of 51.3 to 55.0%. Similar results were also achieved with the changed PMS concentrations (0.2 to 0.5 g/L) and initial pHs (4.0 to 8.0), as the proportions of Cu^{III} oxidation were in the range of 53.6 to 56.7% (Fig. 5*B*) and 53.3 to 62.7% (Fig. 5*C*), respectively. These results indicate that the Cu^{III} oxidation accounted for 51.0 to 63.0% of the phenol degradation in the CuFeMnO/PMS system.

The high-valent metals generated in the CuFeMnO/PMS system also show an impressive reactivity for a wide spectrum of recalcitrant pollutants that cause environmental and public health concerns, such as tetracycline (TC), sulfamethoxazole (SMX), bisphenol A (BPA), nitrobenzene (NB), and benzoic

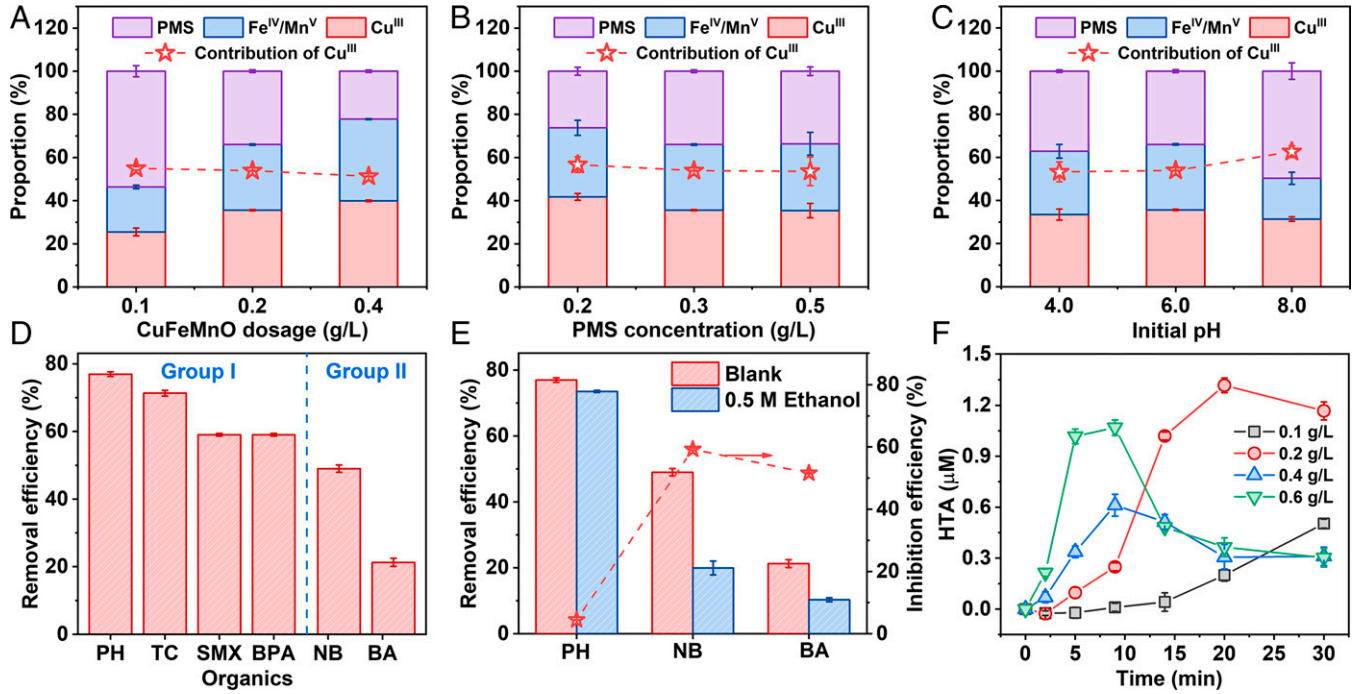

Fig. 5. Contribution of different high-valent metals to pollutant degradation. Effects of (*A*) CuFeMnO dosage, (*B*) PMS concentration, and (*C*) initial pH on the contribution of the different reactive species to the PMSO oxidation. (*D*) The degradation performance of the different pollutants in the CuFeMnO/PMS system. (*E*) The quenching effect of ethanol on the degradation of phenol, NB, and BA. (*F*) The HTA concentration changing profiles in the CuFeMnO/PMS/TA system with the different catalyst dosages. Experimental conditions: [CuFeMnO] = 0.2 g/L, [PMS] = 0.3 g/L, [phenol] = [TC] = [SMX] = [BPA] = [NB] = [BA] = 0.3 mM, [TA] = 1.0 mM, [PMSO] = 0.2 mM, pH = 6.0, T = 25 ± 2 °C.

acid (BA) (Fig. 5*D*). These pollutants can be divided into two groups based on the properties of their functional groups. Group I includes phenol, TC, SMX, and BPA with electron-donating group (e.g., -OH and -NH_2), while group II includes NB and BA with electron-withdrawing group (e.g., -COOH and -NO_2). In contrast to the radical-based AOPs, the highly selective high-valent metals (*SI Appendix*, Table S1) exhibited drastically different degradation efficiencies for the pollutants (e.g., 77.0%, 49.1%, and 21.3% for phenol, NB, and BA, respectively) (Fig. 5*E*). Interestingly, dosing EA, an effective radical quenching agent for •OH and $SO_4^{\bullet-}$, posed distinct inhibition effects on the degradation of the pollutants in the two groups (Fig. 5*E* and *SI Appendix*, Fig. S18). For instance, the inhibition efficiency was 4.4% for phenol (group I), while they were 59.2% and 51.6% for NB and BA (group II), respectively. This quenching experimental result suggests the different degradation mechanisms of the pollutants in the two groups. The high-valent metals were responsible for the degradation of the pollutants in group I, which possessed electron-rich aromatic ring and were susceptible to degradation through electrophilic attack (43, 44), whereas both high-valent metals and •OH were responsible for the degradation of the pollutants in group II, which had electron-deficiency aromatic ring, in which •OH was the secondary oxidant converted from Cu^{III} (eq.1). This also perfectly explains the results in Fig. 5*E* that 59.2% of NB and 51.6% of BA degradation were inhibited by quenching the •OH radical, which is consistent with the contribution of Cu^{III} oxidation (approximately 51.0 to 63.0%).

It is interesting to understand why different reactive species worked in the same reaction system. This phenomenon might be attributed to the competition effect between the pollutants (i.e., phenol, BA, and NB) and the free OH^- ion for Cu^{III}. It is reported that Cu^{III} can readily degrade phenols with electron-donating group but fails to degrade organics with electron-withdrawing group such as NB and BA (36, 45). In this regard, the newly formed Cu^{III} was liable to oxidize phenol in the CuFeMnO/PMS/phenol system but oxidize OH^- to generate •OH when either NB or BA was presented.

$$Cu^{III} + OH^- \rightarrow Cu^{II} + \bullet OH \qquad k = 8 \times 10^3 M^{-1}s^{-1} \text{at pH } 6.0 - 8.0. \qquad [1]$$

Then, the successive generation of Cu^{III} and •OH and their competition effect for pollutant oxidation in the CuFeMnO/PMS system were validated by using terephthalic acid (TA) as the probe, which is widely used for the photoluminescent detection of •OH (46). The fluorescence product of TA hydroxylation, 2-hydroxyterephthalic acid (HTA), was detected at the maximum emission wavelength of 420 nm (*SI Appendix*, Fig. S19), validating the generation of •OH in the CuFeMnO/PMS system. The time-dependent concentration evolutions of HTA at different CuFeMnO dosages were examined. As shown in Fig. 5*F*, the HTA concentration exhibited a monotone increasing tread at low CuFeMnO dosages (ca. 0.1 g/L) but displayed a volcano-like shape at higher CuFeMnO dosages (approximately 0.2 to 0.6 g/L). This result clearly demonstrates that there was a trade-off between the formation of HTA through •OH oxidation and the further oxidative transformation of HTA by the high-valent metals. At high CuFeMnO dosages, the formation rate of the high-valent metals would overwhelm the further conversion of Cu^{III} to •OH, thus a volcano-like shape for HTA formation was observed, and the volcanic peak shifted to earlier times at higher CuFeMnO dosages (Fig. 5*C*). Therefore, these results further confirm the successive generation of the primary high-valent metals and the secondary •OH radical in the CuFeMnO/PMS system. As depicted in *SI Appendix*, Fig. S20, PMS was firstly adsorbed and activated on the surface metal sites on the CuFeMnO catalyst, forming high-valent species (i.e., Cu^{III}, Fe^{IV}, and Mn^{V}) via the one and/or two-electron redox steps (37, 42). Then, the organic pollutant was adsorbed and degraded, and the working reactive species and their contributions were highly dependent on the properties of the target pollutant. For the organics with electron-donating group (e.g., -OH), high-valent metal species were mainly responsible for the pollutant degradation, whereas for the organics with electron-withdrawing group (e.g., -COOH and -NO_2), •OH as the secondary oxidant also played an important role. In such a reaction process, PMS was mainly activated on the Cu site, with the contribution of Cu^{III} or •OH oxidation determined to be approximately 51.0 to 63.0%. However, the exact contribution of Fe^{IV} or Mn^{V} oxidation was unclear due to their similar oxidative features. Afterward, the pristine metal sites (i.e., Cu^{II}, Fe^{III}, and Mn^{III}) were reactivated after the desorption of the oxidized pollutants.

1.6 Pilot-Scale Demonstration and Economic Analysis. The feasibility and stability of this heterogeneous PMS-based AOP were further verified for real water treatment. We first evaluated the performance of the CuFeMnO/PMS system at bench scale in two continuous-flow reactors(Fig. 6*A*). For the reactor packed with the mixture of the CuFeMnO particles and quartz sands, the effluent chemical oxygen demand (COD) concentration drastically decreased from 100.1 to 23.0 mg/L in the initial 12 h and finally below 20 mg/L after stable operation for 188 h (Fig. 6*C*). Meanwhile, phenol could be effectively removed and no residual phenol was detected in the whole period (Fig. 6*C*). In addition, the excellent degradation performances of both COD and phenol were also achieved in the column reactor packed with the CuFeMnO-loaded ceramsites (Fig. 6*D*). Furthermore, the continuous secondary effluent treatment was conducted at pilot scale (Fig. 6*B*). As shown in Fig. 6*E*, the COD concentration in the effluent was below 30 mg/L with the removal efficiency of 50 to 70% during the running period, which stably met level A of the first Class in Discharge Standard of Pollutants for Municipal Wastewater Treatment Plant of China (<50 mg/L COD; GB 18918–2002). It is noteworthy that the COD was mainly removed in the first column (column C), indicating that the current treatment system had spare capacity for increased treatment loading. To evaluate the economical aspect of the CuFeMnO/PMS process, different costs (including energy and chemical consumption) were estimated and are summarized in *SI Appendix*, Table S2. The final cost was estimated to be 126.8 RMB/m^3 of the secondary effluent, which ranked at a moderate level among a variety of AOP-based pilot-scale studies for wastewater treatment (*SI Appendix*, Table S3).

With the above results, we would like to explore the application prospect of the heterogeneous PMS-AOP process for large-scale wastewater treatment in terms of the treatment efficiency, costs, capacity, operational availability, and environmental impact. This five-dimensional evaluation was drawn in a score-radar map (*SI Appendix*, Fig. S21). The CuFeMnO/PMS system, which features simple operation (score 5), could achieve efficient treatment performance for the secondary effluent (score 5), but its large-scale application was unacceptable as yet due to the unaffordable treatment costs (score 2). Our practical experiences show that the treatment costs can be effectively reduced in several facile ways. First, the fixed charge for the catalyst synthesis accounted for approximately 51.3% of the total cost, which can be effectively diluted by extending the running

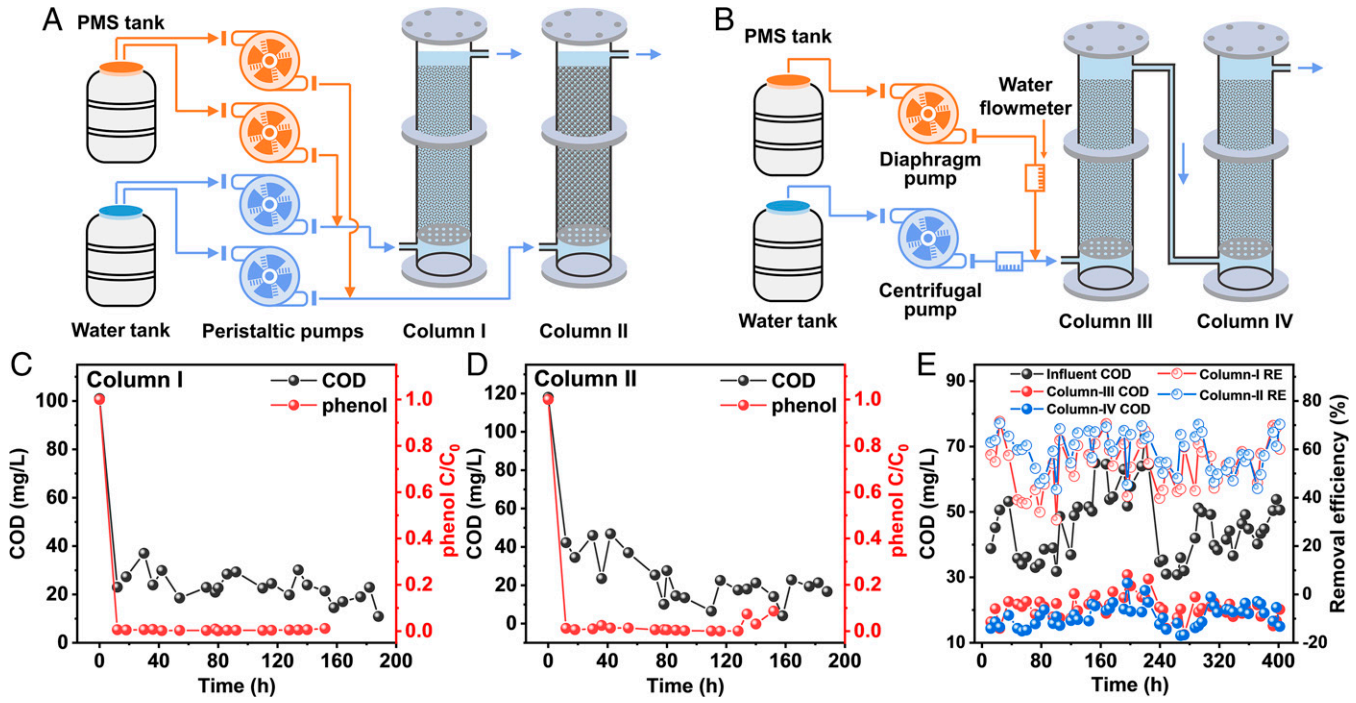

Fig. 6. Pilot-scale demonstration of the CuFeMnO/PMS system. Schematic diagrams of the CuFeMnO-catalyzed PMS process at (*A*) the bench scale and (*B*) the pilot scale. Column I was packed with the mixture of the gram-scale CuFeMnO and quartz sands, column II was packed with the CuFeMnO-loaded ceramsite, columns III and IV were packed with the mixture of the kilogram-scale CuFeMnO and quartz sands. (*C-D*) The degradation performance of phenol and COD in columns I and II, respectively. (*E*) The degradation performance of COD and the corresponding removal efficiencies in columns III and IV. Experimental conditions: (*C-D*) flow rate = 0.63 L/h, hydraulic retention time (HRT) = 2.2 h, [PMS] = 1.4 g/L, pH = 7.0 ± 0.5, (*E*) flow rate = 31.0 L/h, HRT = 4.0 h, [PMS] = 1.8 g/L, pH = 7.0 ± 0.5.

time of the treatment facility. Second, the potential loss of the powdered catalysts greatly limited the treatment capacity (score 2). Loading CuFeMnO on the surface of the supporting material (e.g., ceramsite) can resolve this problem and reduce the treatment cost. Third, the overloaded PMS dosage can be further optimized and substantially reduced. Moreover, the effluent of this pilot-scale facility might pose some negative impacts on the environment (score 3), such as the high-concentration SO_4^{2-} would corrode the cast iron pipes for water distribution (47), and the leached metal ions would be harmful to environment (48). These issues should be addressed before its wide applications.

2. Conclusions

In this work, the nonstoichiometry ternary CuFeMnO spinel oxide with superior PMS-catalytic capacity was prepared for efficient water purification via PMS activation. The outstanding catalytic capacity of the CuFeMnO catalyst was attributed to the rich OVs and the symmetry-breaking sites compared to the benchmark catalysts such as $CuFe_2O_4$, CuO, α-Fe_2O_3, and Mn_2O_3. In the CuFeMnO/PMS system, the high-valent metal species (e.g., Cu^{III}, Fe^{IV}, and Mn^{V}) were primarily generated and •OH as the secondary oxidant converted from Cu^{III} also worked. The specific contributions of these reactive species were highly dependent on the properties of target pollutants (i.e., the electron-donating or withdrawing feature of the functional groups). Furthermore, the continuous-flow reactors packed with the CuFeMnO catalyst were constructed for treating the secondary effluents at both bench and pilot scales. This work demonstrates the feasibility of the heterogeneous PMS-AOP for real water treatment at pilot scale. However, several issues should be addressed before its wide application, such as the high treatment cost, low capacity, and the potential environment impacts.

3. Materials and Methods

3.1 Materials. The chemicals were of analytical grade and used as received in this work. Iron nitrate nonahydrate ($Fe(NO_3)_3•9H_2O$), copper nitrate trihydrate ($Cu(NO_3)_2•3H_2O$), cobalt nitrate hexahydrate ($Co(NO_3)_2•6H_2O$), manganese chloride tetrahydrate ($MnCl_2•4H_2O$), manganese(II, III) oxide (Mn_3O_4), manganese(III) oxide (Mn_2O_3), manganese dioxide (MnO_2), hematite (α-Fe_2O_3), copper oxide (CuO), sodium sulfite (Na_2SO_3), nitrobenzene (NB), benzoic acid (BA), ethanol (EA), and *tert*-butyl alcohol (TBA) were phurchased from Sinopharm Chemical Reagent Co., China. Bismuth nitrate pentahydrate ($Bi(NO_3)_3•5H_2O$), $KHSO_5•0.5KHSO_4•0.5K_2SO_4$ (PMS), cobalt oxide (Co_3O_4), phenol, triclosan (TC), sulfamethoxazole (SMX), bisphenol A (BPA), dimethyl sulfoxide (DMSO), methyl phenyl sulfoxide (PMSO), methyl phenyl sulfone ($PMSO_2$), 2,2,6,6-tetramethyl-4-piperidinol (TEMP), 5,5-dimethyl-1-pyrroline *N*-oxide (DMPO), terephthalic acid (TA), and 2-hydroxyterephthalic acid (HTA) were acquired from Aladdin Chemistry Co., China. All solutions were prepared in deionized water.

3.2 Catalyst Preparation. The gram-scale CuFeMnO catalyst was prepared by a simple coprecipitation method. Specifically, approximately 5 mmol $Cu(NO_3)_2•3H_2O$, 7 mmol $Fe(NO_3)_3•9H_2O$, and 3 mmol $MnCl_2•4H_2O$ were first dissolved in 100 mL deionized water under vigorous stirring. The obtained clear solution was heated to 90 °C and 50 mL alkaline solution containing 70 mmol NaOH was then added. After the mixture was maintained at 90 °C for 60 min, the black precipitate was collected and washed several times to obtain the CuFeMnO oxide. CoFeMnO was synthesized using the same method except $Co(NO_3)_2•6H_2O$ was used instead of $Cu(NO_3)_2•3H_2O$. The similar coprecipitation method was also adopted for the synthesis of $CoFe_2O_4$, $CuFe_2O_4$, and $MnFe_2O_4$, and the molar ratios of Co/Fe, Cu/Fe, and Mn/Fe were all set to 1:2. Furthermore, perovskite $BiFeO_3$ was fabricated according to a sol–gel process reported previously (49).

The kilogram-scale CuFeMnO catalyst for the pilot-scale study was also prepared by the coprecipitation method in a 300-L thickened plastic drum(*SI Appendix*, Fig. S22). The amounts of $Cu(NO_3)_2•3H_2O$, $Fe(NO_3)_3•9H_2O$, $MnCl_2•4H_2O$, and NaOH

were 35, 49, 21, and 490 mol, respectively. The reaction temperature was kept at 80 °C by two heating rods; other procedures were similar to the above-described methods for the synthesis of gram-scale CuFeMnO. Moreover, the CuFeMnO-loaded ceramsite (*SI Appendix*, Fig. S23) was prepared via an impregnation-calcination method. Briefly, approximately 150 g totally washed commercial ceramsites (4 to 5 mm in diameter) were impregnated in the solution containing 25 mmol $Cu(NO_3)_2 \bullet 3H_2O$, 35 mmol $Fe(NO_3)_3 \bullet 9H_2O$, and 15 mmol $MnCl_2 \bullet 4H_2O$. The obtained mixture was then dried at 100 °C and annealed in air at 300 °C for 2 h.

3.3 Characterizations. The XRD patterns of the CuFeMnO catalysts were characterized by a X'Pert MPD X-ray diffractometer (Analytical B.V., the Netherlands) with Cu $K\alpha$ radiation ($\gamma = 1.5418$ Å) in a 2θ range of 10 to 70°. The BET surface areas with N_2 adsorption/desorption isotherms were obtained with an ASAP2460 analyzer (Micromeritics Inc., Norcross, GA). The SEM and HR-TEM images were taken on a Tescan Mira4 instrument (Czech Republic) and an FEI TF20 instrument (Hillsboro, OR), respectively. The H_2-TPR experiments were performed on a Micromeritics AutoChem II 2920 instrument. Prior to each TPR run, approximately a 50-mg sample was pretreated in the He flow at 200 °C for 60 min, it was then cooled down to 50 °C in the He flow. The sample was reduced by 10% H_2/He gas flow at 30 mL/min from 50 to 800 °C with a heating rate of 10 °C/min. The XPS spectra were recorded on an ESCALAB 250Xi instrument (Thermo Fisher Scientific Inc., Waltham, MA), the binding energies of all peaks were referenced to the C 1s line (285.0 eV). The characterization results of the kilogram-scale CuFeMnO including XRD, BET, SEM, HR-TRM, and XPS can be seen in *SI Appendix*, Figs. S24 and S25.

3.4 Pollutant Degradation Experiments. All batch pollutant degradation experiments were conducted at least in duplicate in 50-mL beakers at 25 ± 2 °C under magnetic stirring. In a typical test, a certain mass of CuFeMnO particles was dispersed into an aqueous solution containing desired amounts of target pollutant like phenol and PMS. Before the reaction, the initial pH was adjusted to 6.0 by using 0.5 mM H_2SO_4 or NaOH. The scavenging experiments were conducted with the preaddition of EA, TBA, or DMSO into the reaction system. In the reaction process, approximately 1 mL of reaction suspension was withdrawn and quenched by excess Na_2SO_3, then filtered immediately through a 0.22-μm membrane for organic analysis.

Bench-scale experiments were conducted in two continuous-flow reactors. The reactors were packed with the mixture of the CuFeMnO particles and quartz sands (0.5 to 1.0 mm in diameter) and the CuFeMnO-loaded ceramsite, respectively. The influent for the reactors was obtained from the secondary effluent of the Wangtang Municipal Wastewater Treatment Plant in Hefei, China, with a certain amount of phenol spiked to ensure the accurate analysis of the COD values. The pilot-scale experiment was also conducted in Gaobeidian Municipal Wastewater Treatment Plant in Beijing, China. Two columns packed with the mixture of the kilogram-scale CuFeMnO catalyst and quartz sands were series-connected to achieve a higher treatment capacity (*SI Appendix*, Fig. S26).

3.5 Analysis. The concentrations of the organic compounds were determined by an ultra-high-performance liquid chromatography (UPLC, 1290 Infinity, Agilent Inc., Santa Clara, CA) equipped with a C18 column. A mixture of 0.1% formic acid and acetonitrile (volume/volume= 40%:60%) was adopted as the mobile phase with a flow rate of 0.4 mL/min. The detection wavelength was 273 nm for phenol, TC, SMX, BPA, NB, and BA, 215 nm for PMSO and $PMSO_2$. The concentration of •OH was determined by using TA as the probe agent, TA quickly reacts with •OH ($k_{TA,\ \bullet OH} = 4.4 \times 10^9\ M^{-1}\ s^{-1}$) to form HTA, which can be measured using a luminescence spectrometer (Aqualog-C, Horiba Co., Ann Arbor, MI) with a excitation wavelength at 315 nm (50). NBT with a maximum absorption wavelength at 259 nm was used to determine the concentration of $O_2^{\bullet-}$ with a UV-2450 spectrophotometer (Shimadzu Co., Japan) (50). TOC was measured on a TOC-VCPH analyzer (Multi N/C 2100, Analytik Jena AG, Germany). COD was determined using a model DR-6000 spectrophotometer (Hach Co., Loveland, CO) according to manufacture instructions. The concentrations of the leaching metal ions were measured by an ICP-AES instrument (Optima 7300 DV, PerkinElmer Inc., Waltham, MA). Reactive species were identified on an EPR spectrometer (JES-FA200, JEOL Co., Japan).

3.6 Calculations. DFT calculations were performed using the $DMol^3$ module in Materials Studio (version 2018). Exchange and correlation were treated within the generalized gradient approximation (GGA), using the Perdew-Burke-Ernzerhof (PBE) functional (51). DFT semicore pseudopots together with the double numerical basis set were used for the geometric optimization. The convergence criteria of the geometrical optimization were 1×10^{-5} hartree/atom for energy change, 2×10^{-3} hartree/Å for the gradient, 5×10^{-3} Å for the displacement, and 5×10^{-6} hartree/atom for the self-consistent field tolerance. The electron smearing was 0.01 hartree. Noncovalent forces, such as hydrogen bonding and van der Waals interactions, were described using the empirical correction in the OBS scheme. All calculations were conducted on $CuFeMnO_4$(110) and $CuFe_2O_4$(110). These two surfaces were modeled as a five-layer p(2 × 2) slab with a 15 Å vacuum gap along the z direction. Three top layers were allowed to relax, and the bottom layers were fixed. A Monkhorst-Pack (2 × 2 × 1) k-point was used to sample the Brillouin zone.

Data Availability. All study data are included in the article and/or supporting information.

ACKNOWLEDGMENTS. This work is supported by the National Natural Science Foundation of China (22106159, 52192684 and 51821006) and China Postdoctoral Science Foundation (2021M693073). The numerical calculations have been performed on the supercomputing system in the Supercomputing Center of University of Science and Technology of China.

Author affiliations: [a]CAS Key Laboratory of Urban Pollutant Conversion, Department of Environmental Science and Engineering, University of Science and Technology of China, Hefei, 230026, China; [b]Ganjiang Innovation Academy, Chinese Academy of Sciences, Ganzhou, 341000, China; [c]School of Resources and Environmental Engineering, Hefei University of Technology, Hefei, 230009, China; [d]Key Laboratory of Drinking Water Science and Technology, Research Center for Eco-Environmental Sciences, University of Chinese Academy of Sciences, Chinese Academy of Sciences, Beijing, 100085, China; and [e]School of Environmental Science and Engineering, Huazhong University of Science and Technology, Wuhan, 430074, China

1. Z. Yang, J. Qian, A. Yu, B. Pan, Singlet oxygen mediated iron-based Fenton-like catalysis under nanoconfinement. *Proc. Natl. Acad. Sci. U.S.A.* **116**, 6659–6664 (2019).
2. F. Chen *et al.*, Efficient decontamination of organic pollutants under high salinity conditions by a nonradical peroxymonosulfate activation system. *Water Res.* **191**, 116799 (2021).
3. M. Huang, T. Zhou, X. Wu, J. Mao, Distinguishing homogeneous-heterogeneous degradation of norfloxacin in a photochemical Fenton-like system (Fe_3O_4/UV/oxalate) and the interfacial reaction mechanism. *Water Res.* **119**, 47–56 (2017).
4. F. Ghanbari, M. Moradi, Application of peroxymonosulfate and its activation methods for degradation of environmental organic pollutants: Review. *Chem. Eng. J.* **310**, 41–62 (2017).
5. X. Mi *et al.*, Almost 100% peroxymonosulfate conversion to singlet oxygen on single-atom CoN_{2+2} sites. *Angew. Chem. Int. Ed. Engl.* **60**, 4588–4593 (2021).
6. P. Li *et al.*, Defect-engineered Co_3O_4 with porous multishelled hollow architecture enables boosted advanced oxidation processes. *Appl. Catal. B* **298**, 120596 (2021).
7. W. Wang *et al.*, The confined interlayer growth of ultrathin two-dimensional Fe_3O_4 nanosheets with enriched oxygen vacancies for peroxymonosulfate activation. *ACS Catal.* **11**, 11256–11265 (2021).
8. L. Chen *et al.*, Degradation of acetaminophen by activated peroxymonosulfate using $Co(OH)_2$ hollow microsphere supported titanate nanotubes: Insights into sulfate radical production pathway through $CoOH^+$ activation. *Chem. Eng. J.* **406**, 126877 (2021).
9. Y. Wang *et al.*, Degradation of benzophenone-4 by peroxymonosulfate activated with microwave synthesized well-distributed $CuBi_2O_4$ microspheres: Theoretical calculation of degradation mechanism. *Appl. Catal. B* **290**, 120048 (2021).
10. Y. Peng *et al.*, Activation of peroxymonosulfate (PMS) by spinel ferrite and their composites in degradation of organic pollutants: A Review. *Chem. Eng. J.* **414**, 128800 (2021).
11. Q. Dai, Z. Zhang, T. Zhan, Z. T. Hu, J. Chen, Catalytic ozonation for the degradation of 5-sulfosalicylic acid with spinel-type $ZnAl_2O_4$ prepared by hydrothermal, sol-gel, and coprecipitation methods: A comparison study. *ACS Omega* **3**, 6506–6512 (2018).
12. O. A. Sánchez, J. L. Rodríguez, J. M. Barrera-Andrade, R. Borja-Urby, M. A. Valenzuela, High performance of Ag/$BiVO_4$ photocatalyst for 2,4-Dichlorophenoxyacetic acid degradation under visible light. *Appl. Catal. A Gen.* **600**, 117625 (2020).
13. C. Li *et al.*, Clinoptilolite mediated activation of peroxymonosulfate through spherical dispersion and oriented array of $NiFe_2O_4$: Upgrading synergy and performance. *J. Hazard. Mater.* **407**, 124736 (2021).
14. M. Ding *et al.*, Heterogeneous $Fe_2CoTi_3O_{10}$-MXene composite catalysts: Synergistic effect of the ternary transition metals in the degradation of 2,4-dichlorophenoxyacetic acid based on peroxymonosulfate activation. *Chem. Eng. J.* **378**, 122177 (2019).
15. Z. Y. Guo *et al.*, Mn-O covalency governs the intrinsic activity of Co-Mn spinel oxides for boosted peroxymonosulfate activation. *Angew. Chem. Int. Ed. Engl.* **60**, 274–280 (2021).
16. D. Yu *et al.*, New insights into Sr-O bonds enhances Co/Fe catalytic activity in SrCoFe perovskite for boosted peroxymonosulfate activation. *Chem. Eng. J.* **426**, 131525 (2021).
17. W. Sun *et al.*, Oxygen vacancy mediated $La_{1-x}Ce_xFeO_{3-\delta}$ perovskite oxides as efficient catalysts for CWAO of acrylic acid by A-site Ce doping. *Appl. Catal. B* **245**, 20–28 (2019).

18. H. Zhang, C. Li, L. Lyu, C. Hu, Surface oxygen vacancy inducing peroxymonosulfate activation through electron donation of pollutants over cobalt-zinc ferrite for water purification. *Appl. Catal. B* **270**, 118874 (2020).
19. K. S. Sing, Reporting physisorption data for gas/solid systems with special reference to the determination of surface area and porosity. *Pure Appl. Chem.* **57**, 603–619 (1985).
20. G. P. Anipsitakis, D. D. Dionysiou, Radical generation by the interaction of transition metals with common oxidants. *Environ. Sci. Technol.* **38**, 3705–3712 (2004).
21. Z. Wang, R. Lin, Y. Huo, H. Li, L. Wang, Formation, detection, and function of oxygen vacancy in metal oxides for solar energy conversion. *Adv. Funct. Mater.* **32**, 2109503 (2022).
22. Y. Zhang *et al.*, Morphology-dependent catalytic properties of nanocupric oxides in the Rochow reaction. *Nano Res.* **11**, 804–819 (2017).
23. E. R. Stobbe, B. A. de Boer, J. W. Geus, The reduction and oxidation behaviour of manganese oxides. *Catal. Today* **47**, 161–167 (1999).
24. Y. Jian *et al.*, In-depth understanding of the morphology effect of α-Fe_2O_3 on catalytic ethane destruction. *ACS Appl. Mater. Interfaces* **11**, 11369–11383 (2019).
25. C. Chen *et al.*, Reduction of nanostructured CuO bundles: Correlation between microstructure and reduction properties. *Cryst. Growth Des.* **8**, 3549–3554 (2008).
26. M. Huang *et al.*, Ultrafast O_2 activation by copper oxide for 2,4-dichlorophenol degradation: The size-dependent surface reactivity. *Chin. Chem. Lett.* **31**, 2769–2773 (2020).
27. H. Li, J. Zhao, L. Luo, J. Du, J. Zeng, Symmetry-breaking sites for activating linear carbon dioxide molecules. *Acc. Chem. Res.* **54**, 1454–1464 (2021).
28. K. Zhang *et al.*, Efficient peroxymonosulfate activation in electron-rich/poor reaction sites induced by copper-iron oxide heterojunctions/interfaces: Performance and mechanism. *Chem. Eng. J.* **423**, 129971 (2021).
29. G. X. Huang, C. Y. Wang, C. W. Yang, P. C. Guo, H. Q. Yu, Degradation of bisphenol A by peroxymonosulfate catalytically activated with $Mn_{1.8}Fe_{1.2}O_4$ nanospheres: Synergism between Mn and Fe. *Environ. Sci. Technol.* **51**, 12611–12618 (2017).
30. Z. Chen, L. Wang, H. Xu, Q. Wen, Efficient heterogeneous activation of peroxymonosulfate by modified $CuFe_2O_4$ for degradation of tetrabromobisphenol A. *Chem. Eng. J.* **389**, 124345 (2020).
31. H.-H. Kim *et al.*, Activation of hydrogen peroxide by a titanium oxide-supported iron catalyst: Evidence for surface Fe(IV) and its selectivity. *Environ. Sci. Technol.* **54**, 15424–15432 (2020).
32. L. Zhu *et al.*, Designing 3D-MoS_2 sponge as excellent cocatalysts in advanced oxidation processes for pollutant control. *Angew. Chem. Int. Ed. Engl.* **59**, 13968–13976 (2020).
33. M. Huang *et al.*, Strong metal-support interaction between carbon nanotubes and Mn-Fe spinel oxide in boosting peroxymonosulfate activation: Underneath mechanisms and application. *Chem. Eng. J.* **429**, 132372 (2022).
34. J. Huang, S. Zhong, Y. Dai, C.-C. Liu, H. Zhang, Effect of MnO_2 phase structure on the oxidative reactivity toward bisphenol A degradation. *Environ. Sci. Technol.* **52**, 11309–11318 (2018).
35. Y. Gao, Z. Chen, Y. Zhu, T. Li, C. Hu, New insights into the generation of singlet oxygen in the metal-free peroxymonosulfate activation process: Important role of electron-deficient carbon atoms. *Environ. Sci. Technol.* **54**, 1232–1241 (2020).
36. Y. Wang *et al.*, Natural polyphenols enhanced the Cu(II)/peroxymonosulfate (PMS) oxidation: The contribution of Cu(III) and $HO^{\bullet}$. *Water Res.* **186**, 116326 (2020).
37. Y. Gao *et al.*, Enhanced peroxymonosulfate activation via complexed Mn(II): A novel non-radical oxidation mechanism involving manganese intermediates. *Water Res.* **193**, 116856 (2021).
38. S. Enami, Y. Sakamoto, A. J. Colussi, Fenton chemistry at aqueous interfaces. *Proc. Natl. Acad. Sci. U.S.A.* **111**, 623–628 (2014).
39. P. Amels, H. Elias, K.-J. Wannowius, Kinetics and mechanism of the oxidation of dimethyl sulfide by hydroperoxides in aqueous medium study on the potential contribution of liquid-phase oxidation of dimethyl sulfide in the atmosphere. *J. Chem. Soc., Faraday Trans.* **93**, 2537–2544 (1997).
40. Y. Zong *et al.*, Enhanced oxidation of organic contaminants by iron(II)-activated periodate: The significance of high-valent iron-oxo species. *Environ. Sci. Technol.* **55**, 7634–7642 (2021).
41. V. A. Larson, B. Battistella, K. Ray, N. Lehnert, W. Nam, Iron and manganese oxo complexes, oxo wall and beyond. *Nat. Rev. Chem.* **4**, 404–419 (2020).
42. X. Liu *et al.*, Ferric ion promoted degradation of acetaminophen with zero-valent copper activated peroxymonosulfate process. *Chem. Eng. J.* **426**, 131679 (2021).
43. M.-J. Kang *et al.*, Mechanistic insight into the aromatic hydroxylation by high-valent iron(IV)-oxo porphyrin π-cation radical complexes. *J. Org. Chem.* **72**, 6301–6304 (2007).
44. A. Decker *et al.*, Spectroscopic and quantum chemical studies on low-spin Fe^{IV}=O complexes: Fe-O bonding and its contributions to reactivity. *J. Am. Chem. Soc.* **129**, 15983–15996 (2007).
45. Y. Feng *et al.*, Factors and mechanisms that influence the reactivity of trivalent copper: A novel oxidant for selective degradation of antibiotics. *Water Res.* **149**, 1–8 (2019).
46. E. M. Rodríguez, U. von Gunten, Generation of hydroxyl radical during chlorination of hydroxyphenols and natural organic matter extracts. *Water Res.* **177**, 115691 (2020).
47. J. Hu *et al.*, Impacts of water quality on the corrosion of cast iron pipes for water distribution and proposed source water switch strategy. *Water Res.* **129**, 428–435 (2018).
48. K. H. Vardhan, P. S. Kumar, R. C. Panda, A review on heavy metal pollution, toxicity and remedial measures: Current trends and future perspectives. *J. Mol. Liq.* **290**, 111197 (2019).
49. W. Luo *et al.*, Efficient removal of organic pollutants with magnetic Nanoscaled $BiFeO_{(3)}$ as a reusable heterogeneous fenton-like catalyst. *Environ. Sci. Technol.* **44**, 1786–1791 (2010).
50. L. Ye, J. Liu, Z. Jiang, T. Peng, L. Zan, Facets coupling of BiOBr-g-C_3N_4 composite photocatalyst for enhanced visible-light-driven photocatalytic activity. *Appl. Catal. B* **142**, 1–7 (2013).
51. J. P. Perdew, K. Burke, M. Ernzerhof, Generalized gradient approximation made simple. *Phys. Rev. Lett.* **78**, 1396 (1997).